Received: 10 January 2022 | Revised: 17 March 2022 | Accepted: 25 March 2022

DOI: 10.1002/hbm.25855

RESEARCH ARTICLE

WILEY

Mapping of whole-cerebrum resting-state networks using ultra-high resolution acquisition protocols

Seong Dae Yun[1] | Patricia Pais-Roldán[1] | Nicola Palomero-Gallagher[2,3,4] | N. Jon Shah[1,5,6,7]

[1]Institute of Neuroscience and Medicine–4, Medical Imaging Physics, Forschungszentrum Jülich, Jülich, Germany

[2]Institute of Neuroscience and Medicine–1, Structural and Functional Organisation of the Brain, Forschungszentrum Jülich, Jülich, Germany

[3]C. & O. Vogt Institute for Brain Research, Heinrich-Heine-University, Düsseldorf, Germany

[4]Department of Psychiatry, Psychotherapy and Psychosomatics, Medical Faculty, RWTH Aachen, Aachen, Germany

[5]Institute of Neuroscience and Medicine–11, Molecular Neuroscience and Neuroimaging, JARA, Forschungszentrum Jülich, Jülich, Germany

[6]JARA – BRAIN – Translational Medicine, Aachen, Germany

[7]Department of Neurology, RWTH Aachen University, Aachen, Germany

Correspondence
N. Jon Shah, Institute of Neuroscience and Medicine–4, Forschungszentrum Jülich, 52425 Jülich, Germany.
Email: n.j.shah@fz-juelich.de

Abstract

Resting-state functional magnetic resonance imaging (fMRI) has been used in numerous studies to map networks in the brain that employ spatially disparate regions. However, attempts to map networks with high spatial resolution have been hampered by conflicting technical demands and associated problems. Results from recent fMRI studies have shown that spatial resolution remains around $0.7 \times 0.7 \times 0.7$ mm^3, with only partial brain coverage. Therefore, this work aims to present a novel fMRI technique that was developed based on echo-planar-imaging with keyhole (EPIK) combined with repetition-time-external (TR-external) EPI phase correction. Each technique has been previously shown to be effective in enhancing the spatial resolution of fMRI, and in this work, the combination of the two techniques into TR-external EPIK provided a nominal spatial resolution of $0.51 \times 0.51 \times 1.00$ mm^3 (0.26 mm^3 voxel) with whole-cerebrum coverage. Here, the feasibility of using half-millimetre in-plane TR-external EPIK for resting-state fMRI was validated using 13 healthy subjects and the corresponding reproducible mapping of resting-state networks was demonstrated. Furthermore, TR-external EPIK enabled the identification of various resting-state networks distributed throughout the brain from a single fMRI session, with mapping fidelity onto the grey matter at 7T. The high-resolution functional image further revealed mesoscale anatomical structures, such as small cerebral vessels and the internal granular layer of the cortex within the postcentral gyrus.

KEYWORDS
EPIK, half-mm in-plane resolution, resting-state fMRI, TR-external phase correction, whole-cerebrum

1 | INTRODUCTION

Since the first demonstration of blood-oxygenated-level-dependent (BOLD) contrast using MRI (Ogawa et al., 1990), fMRI, as it has become known, has been widely used to explore brain function under either resting-state or evoked by a stimulus-driven paradigm. Task-evoked fMRI detects functional signals involved with a specific given task, which reflect only a small fraction of the brain's overall activity

(Smitha et al., 2017). In contrast, resting-state fMRI (rs-fMRI) focuses on spontaneous neuronal activity fluctuating at very low frequencies (<0.1 Hz), by which correlated brain areas in disparate regions, termed 'resting-state network (RSN)', can be identified (Biswal et al., 1995, 1997; Smitha et al., 2017; van den Heuvel & Hulshoff Pol, 2010). Thus, rs-fMRI has been employed by many groups for the investigation of overall brain function and its underlying connectivity (Smitha et al., 2017). In addition, the task-free acquisition of rs-fMRI allows various neurological issues to be studied in patients (e.g., cognitive dysfunction, psychiatric disorders, consciousness, etc.) or young children (e.g., neonates, infants, etc.), who either have difficulties or simply cannot comply with designed paradigms (Adhikari et al., 2019; Heine et al., 2012; Zhang et al., 2019).

Recent advances in fMRI techniques enable the depiction of neuronal activation with a submillimetre voxel size. Previously, several fMRI studies have employed high-resolution imaging techniques to measure the fMRI signal with a cortical depth-dependence (referred to as 'laminar fMRI'; e.g., Huber et al., 2017; Yu et al., 2014). However, most of these high-resolution laminar fMRI investigations of activation profiles through the cortex have only targeted functional activation evoked by a task paradigm in a particular brain region (Chai et al., 2020; Guidi et al., 2016; Huber et al., 2015; Kashyap et al., 2018; van Mourik et al., 2019), leaving the laminar dynamics underlying the resting-state largely unexplored. This is mainly due to the technical limitations of the current fMRI techniques, which are only able to offer submillimetre voxel size with limited brain coverage.

There have been numerous attempts to improve the spatiotemporal resolution of fMRI, including the use of a reduced field-of-view (FOV) (Heidemann et al., 2012; Kemper et al., 2018; Zimmermann et al., 2011) or the use of non-Cartesian and random sampling trajectories (Fang et al., 2016; Jiang et al., 2018; Kasper et al., 2019). Although a reduced FOV can usually achieve a higher spatial resolution than full-FOV schemes, the restricted FOV has a critical limiting factor in brain coverage. The non-Cartesian approaches improve spatial resolution by employing a more efficient *k*-space sampling scheme, such as radial or spiral trajectories (Jiang et al., 2018; Kasper et al., 2019); however, off-resonance artefacts, typically resulting from these trajectories, render a robust localisation of functional activity difficult without the application of an additional correction method (Kasper et al., 2019). Although the random sampling method also offers more robust image reconstruction, leading to a highly accelerated acquisition, its complex image reconstruction can introduce distortions to functional time-series data, resulting in the reduction or slight sinusoidal variations of BOLD amplitudes (Fang et al., 2016; Zong et al., 2014); it is noted, however, that the key HRF characteristics in the aforementioned study by Fang et al. are well preserved.

For the reasons described above, full-FOV Cartesian sampling methods are still widely used, and of these, echo-planar imaging (EPI) (Mansfield, 1977) is the most commonly implemented method for submillimetre-resolution fMRI studies (Kay et al., 2019; Koizumi et al., 2019; Kok et al., 2016; Sharoh et al., 2019; van Dijk et al., 2020). However, the spatial resolution achieved in several recent works has remained around $0.7 \times 0.7 \times 0.7\ mm^3$, and most methods are only able to provide limited brain coverage.

This work presents a novel fMRI methodology, providing a half-millimetre in-plane resolution with whole-cerebrum coverage. The imaging method was developed based on the combination of 'TR-external EPI phase correction' (Wielopolski et al., 1998; Yun & Shah, 2020) with 'EPI with keyhole' (EPIK) (Caldeira et al., 2019; Shah, 2015; Shah et al., 2019; Shah & Zilles, 2003, 2004; Yun et al., 2013, Yun & Shah, 2019, Yun & Weidner, 2019, 2020; Yun & Shah, 2017, 2019; Zaitsev et al., 2001, 2005), both of which have been shown to be effective in improving the spatial resolution and brain coverage while maintaining comparable BOLD detection performance when compared to a standard EPI method (Caldeira et al., 2019; Shah et al., 2019; Yun et al., 2013; Yun & Shah, 2017, 2019, 2020). The developed imaging method is termed 'TR-external EPIK' (Yun et al., 2020; Yun & Shah, 2019).

This work focuses on the evaluation of a half-millimetre protocol implemented using TR-external EPIK at 7T. A qualitative inspection of the achieved spatial resolution was performed by identifying meso-scale anatomical structures in reconstructed images. The protocol was employed in rs-fMRI to demonstrate high-resolution mapping of activated voxels in a number of RSNs distributed widely over the brain. Furthermore, rs-fMRI data were acquired from a group of subjects to verify the robust detection of functional signals using TR-external EPIK. The imaging performance of TR-external EPIK was evaluated by comparison with the imaging parameters of previously published submillimetre-resolution fMRI studies.

2 | MATERIALS AND METHODS

2.1 | TR-external EPIK

Figure 1a shows a sequence diagram of the proposed TR-external EPIK method. The entire TR loop consists of two excitation sub-loops. The first excitation sub-loop (α_{PC}; TR_{PC}) acquires three navigator echoes for the correction of *N*/2 ghost artefacts, whereas the second excitation sub-loop (α_{Main}; TR_{Main}) performs echo-planar readout according to the EPIK scheme (Figure 1b). The lack of navigator echoes in the second sub-loop facilitates a decreased minimum TE, enabling a larger imaging matrix size for a higher spatial resolution at any given TE. As demonstrated previously, the flip angles for the first and second sub-loops were determined as 9° and 90° (Yun & Shah, 2020).

Figure 1b illustrates a schematic representation of three-shot EPIK with respect to the temporal indices. For each measurement, the central *k*-space is fully sampled with a Nyquist rate ($\Delta k_y = 1/FOV$), which ensures an optimum signal-to-noise ratio (SNR) and contrast-to-noise ratio for every single time frame subsequently reconstructed. However, the peripheral *k*-space is sparsely sampled, as in multi-shot EPI ($\Delta k_y' = 3/FOV$). Crucially, the peripheral *k*-space is continually updated every three shots according to a sliding-window reconstruction scheme (Noll et al., 1991). This acquisition scheme can achieve a higher *apparent* temporal resolution than the community-standard

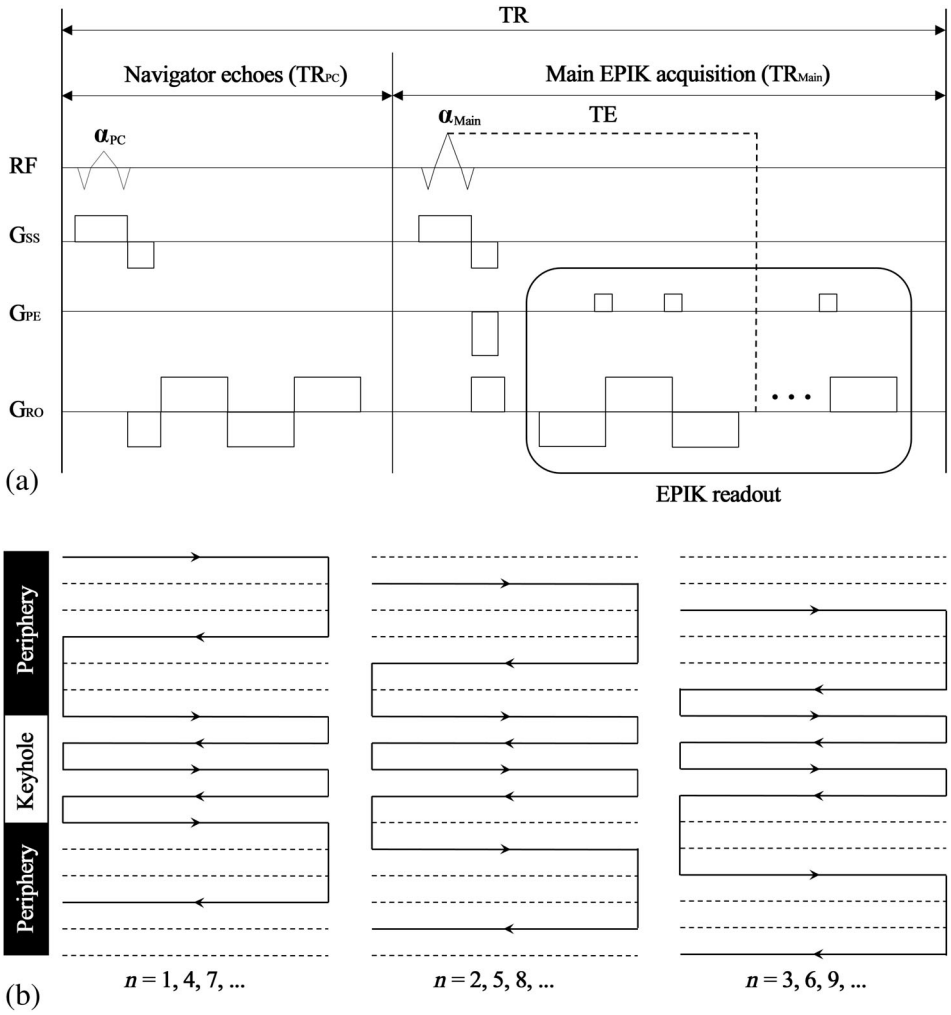

FIGURE 1 Echo-planar-imaging with keyhole (EPIK) with repetition-time-external (TR-external) EPI phase correction (TR-external EPIK). (a) Schematic representation of TR-external EPIK and (b) detailed description of *k*-space sampling in EPIK. Each TR of TR-external EPIK consists of a low-flip angle excitation sub-loop (α_{PC}; TR_{PC}) for navigator echoes and the main excitation sub-loop (α_{Main}; TR_{Main}) for the EPIK readout (outlined by the rectangle in a). The EPIK scan was acquired according to the *k*-space trajectories shown in b, in which the solid and dashed lines indicate lines to be sampled and to be skipped, respectively. The first *k*-space line acquired in the first, second and third scans (i.e., $n = 1$, 2 and 3) was line 1, 2 and 3, respectively. The first line acquired became 1 again for the fourth scan ($n = 4$), in which the original line 1 was discarded, ensuring a refreshed periphery

method, EPI. This work employs 48 central *k*-space lines for the keyhole region (Shah et al., 2019; Yun et al., 2013, 2020; Yun & Shah, 2017, 2019; Zaitsev et al., 2001). A more detailed description of the features of EPIK is given in Supporting Information (see 5.1. with Figure S1).

The above TR-external EPIK scheme enabled a half-millimetre protocol with the following parameters: TR = 3500 (i.e., 15.7 ms for TR_{PC} + 3484.3 ms for TR_{Main}), TE = 22 ms, FOV = 210 × 210 mm^2, matrix = 408 × 408 × 108 slices (0.51 × 0.51 × 1.0 mm^3), partial Fourier = 5/8, three-fold in-plane/three-fold inter-plane (GRAPPA/multi-band) acceleration (Griswold et al., 2002; Larkman et al., 2001; Setsompop et al., 2012), bandwidth = 721 Hz/Px and αPC/αMain = 9°/90°. Here, an isovoxel protocol (0.63 × 0.63 × 0.63 mm^3) was also configured with the same TR, TE, FOV and acceleration conditions as above, but with a different matrix size: 336 × 336 × 123 slices. A 3D anatomical image was acquired using a T_1-weighted magnetisation-prepared, rapid gradient echo (MP2RAGE) pulse sequence with the following parameters: matrix size = 376 × 400 with 256 sagittal slices (0.6 mm isotropic), $TR/TI_1/TI_2/TE$ = 4440/840/2370/2.08 ms. The above imaging configuration was employed on a Siemens Magnetom Terra 7T scanner with a single-channel Tx/32-channel Rx Nova medical coil supplied by the manufacturer.

2.2 | In vivo measurements

All in vivo measurements in this work were performed on healthy volunteers screened, in addition, for neurological or psychiatric illnesses. After a complete description of the study, written informed consent was obtained before scanning. The local institutional review board (RWTH Aachen University, Germany) approved the study protocol (EK 346/17), screening questionnaires and consent forms. Eighteen healthy volunteers (14 males, 4 females; mean age, 30.22 years; range, 23–47 years) were recruited for the study. In order to control for the effect of physiological noise, respiratory and cardiac signals were recorded using a pneumatic belt positioned around the subject's chest and a pulse-oximetre placed on the second, third or fourth finger of the left hand.

2.3 | Resting-state fMRI and data analysis

The data acquisition consisted of four dummy scans, to reach a steady-state, and 172 scans to acquire 10-min of rs-fMRI data. Functional data were pre-processed using MATLAB (MathWorks, Inc.) and AFNI (Analysis of Functional NeuroImages, NIH, Bethesda, MD) to

perform slice-timing correction, realignment, regression of cardio-respiratory signals, regression of the mean white-matter and mean CSF signal, and temporal filtering (0.005–0.12 Hz band-pass) with regression of motion parameters. In addition, the effect of large pial vessels on functional activation was reduced using a previously described method (Curtis et al., 2014; Menon, 2002), whereby the maximum likelihood estimator is initially derived from a fit of the phase image to the magnitude image using the chi-squared function minimisation (Press et al., 1992), and the estimator is then subtracted from the magnitude image to remove signal components presumably attributed to field inhomogeneities from large veins. The structural data were co-registered to the functional images using FreeView with a linear transformation (FsTutorial, MultiModalRegistration, https://surfer.nmr.mgh.harvard.edu). Data sets from five subjects were excluded for the following reasons: one subject's data set showed very high motion displacement (i.e., mean displacement >0.5 mm), which possibly led to the poor functional activation of the studied networks, two subjects' data sets had very noisy signals in the recorded physiological data (i.e., respiratory and cardiac signals) leading to unreliable data pre-processing, and the other two subjects' data sets had only partially recorded physiological data due to systematic difficulties.

Independent component analysis (ICA) with Melodic (FSL, FMRIB Software Library, Oxford, UK) was individually performed for each subject's functional data, that is, without concatenation of all subjects' data sets. Based on the standard routine of FSL, the optimal number of ICA components was determined as being 74 and 76 for the data sets from the 13 subjects. This analysis quantified the probability of the voxel belonging to a given network. From all the automatically detected components for each subject, the best matching components to present RSNs were manually selected. The activated voxels were obtained with a statistical threshold (probability ≥.5).

2.4 | Group analysis: Reproducibility

The quality of the functional scans was assessed by inspecting the image SNR. The mean signal value was calculated by extracting the brain using the standard SPM segmentation routine (Wellcome Department of Imaging Neuroscience, UCL, London, UK) and obtaining its mean value. The standard deviation of noise was obtained from regions of interest (ROIs) located at the four corners of the reconstructed images. The noise ROI at each corner was determined with a sufficiently large matrix size (40 × 60 voxels) so as to include enough noise sources from the background while avoiding the inclusion of structural noise (e.g., *N*/2 ghosts). The calculation was performed for each temporal frame of each subject (i.e., 172 temporal frames per subject), and the mean ± SD SNR across the temporal dimension was obtained.

In order to check the reproducibility of the mapping of the RSNs, five representative subjects showing the same RSN were selected, and their activated voxels were individually compared in the space of their subject-specific mean functional scans. Furthermore, the prevalence of each RSN in the data was quantified as the number of subjects in which the RSN was identified. Furthermore, a second-level analysis was carried out to inspect a group-wise network-specific activation which was obtained by first averaging unthresholded RSN maps from each subject and then thresholding the averaged maps with mean probability. This involved spatial normalisation to a common template in MNI (Montreal Neurological Institute) space. Here, the spatial correlation between the RSNs from our data and those from reference templates (Shirer et al., 2012) was also computed.

2.5 | Evaluation of imaging performance

In order to provide insight into the spatial resolution and brain coverage provided by TR-external EPIK, its imaging performance was evaluated by directly comparing the imaging parameters employed in several previous submillimetre-resolution fMRI studies (Berman et al., 2021; Fracasso et al., 2018; Guidi et al., 2020; Heidemann et al., 2012; Huber et al., 2020; Kasper et al., 2019; Kay et al., 2019; Kemper et al., 2018; Koizumi et al., 2019; Kok et al., 2016; Sharoh et al., 2019; van Dijk et al., 2020). The parameters compared were: (1) in-plane voxel size (mm), (2) normalised in-plane FOV (mm), calculated by $\sqrt{FOV_x \cdot FOV_y}$, (3) slice thickness (mm), (4) normalised slice throughput, calculated by the number of slices provided per 3.5 s of TR, (5) volume of a single voxel (mm^3), (6) number of voxels per temporal volume (M), calculated by the normalised slice throughput × in-plane matrix sizes, (7) TE and (8) volumetric TR.

3 | RESULTS

3.1 | Functional scan with a half-millimetre in-plane resolution

Figure 2 shows reconstructed images obtained from the half-millimetre protocol. Here, the surface of the grey matter (GM) and the white matter (WM) was extracted from all the acquired slices and rendered in 3D (Figure 2a), effectively demonstrating the distinct contrasts between the GM and WM with near whole-brain coverage provided by TR-external EPIK. The 3D rendered surface of GM and WM was obtained using a 3D visualisation tool, ParaView (www.paraview.org).

For more detailed visual inspection, sectional slices (axial, coronal and sagittal) were taken from a single-volume functional scan, as shown in Figure 2b,d,e. Figure 2b shows four of the 108 axial slices; the entire reconstructed slices can be found in Supporting Information (see Figure S2). From the axial slices, specific brain regions were chosen (marked by white rectangles: r_1–r_4) in which the following mesoscale anatomical structures can be observed (Figure 2c): small cerebral vessels (red arrows in r_2) or the internal granular layer of the cortex (yellow arrows) located on the anterior wall of the postcentral gyrus (r_1), on the Heschl gyrus (r_3) or within the calcarine sulcus (r_4). Here, the position of layer IV, highlighted with a white line, can be found in

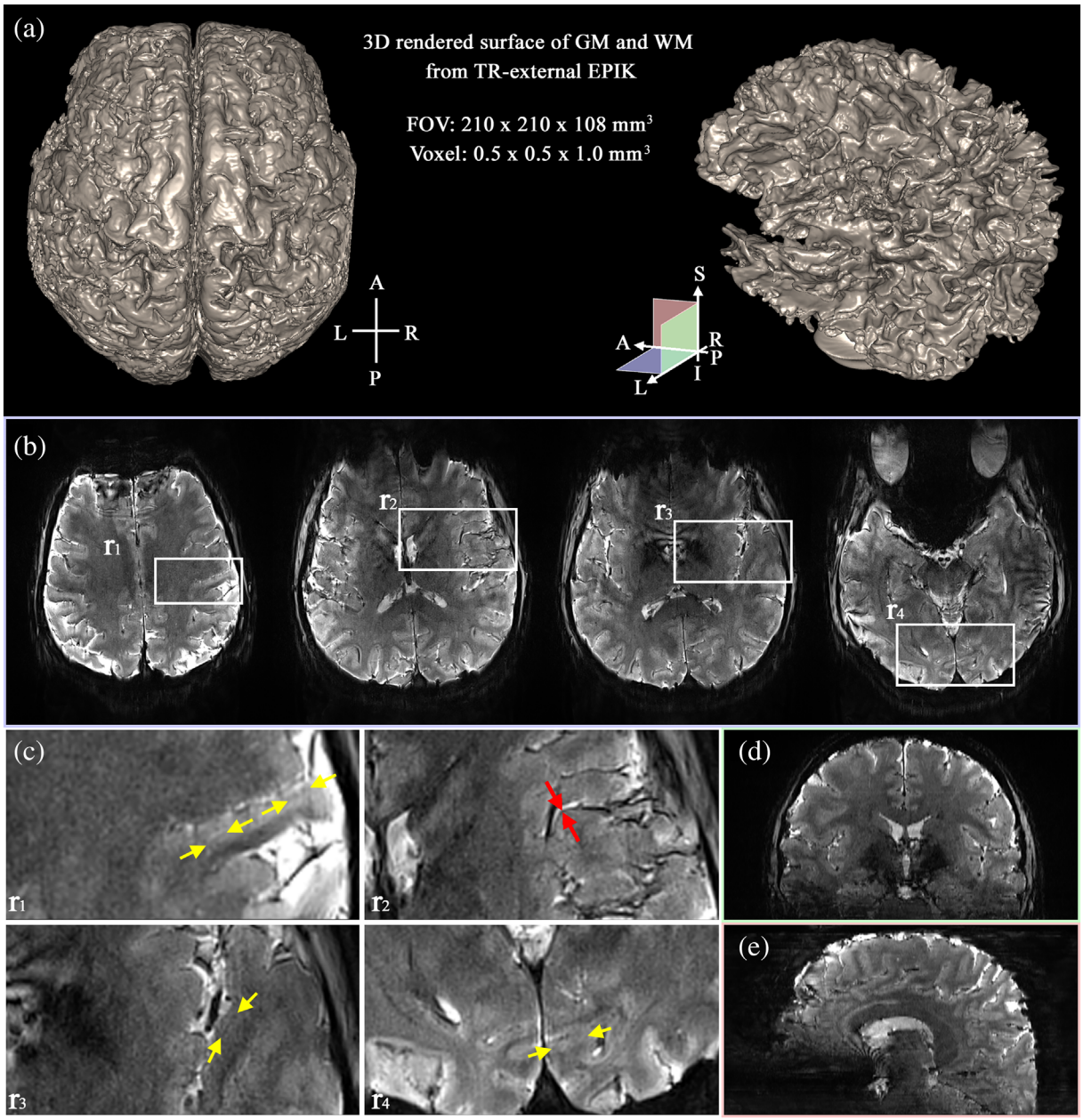

FIGURE 2 Reconstructed images from the half-millimetre (0.51 × 0.51 mm^2) protocol. (a) 3D rendered surface of the grey matter (GM; left) and white matter (WM; right) obtained from TR-external EPIK, (b) four representative slices, selected from a set of 108 axial slices, (c) enlarged depiction of the regions of interest (ROIs) marked by the white rectangles in b (r_1–r_4), where the following mesoscale anatomical structures can be observed: small cerebral vessels (r_2) or the internal granular layer of the cortex within the postcentral gyrus (r_1), the Heschl gyrus (r_3) and the calcarine sulcus (r_4) and (d,e) resliced and reconstructed coronal and sagittal views of the 108 axial slices demonstrating the extensive brain coverage provided by TR-external EPIK. Note that cortical ribbons are clearly visible even in the resliced images

the Supporting Information Section 5.3 (see Figure S3), in which the resolution performance of TR-external EPIK was further verified with a high-resolution phantom (see Figure S4). The complete extent of the brain covered by TR-external EPIK can be verified from the coronal and sagittal images (Figure 2d,e). It is important to note that the cortical ribbon can even be seen clearly in these resliced images. In addition, these depictions also show that all slices were reconstructed without any significant inter-slice artefacts, which can sometimes occur as a result of the multi-band reconstruction (McNabb et al., 2020). The signal behaviour along the direction in which multi-band acceleration was applied (i.e., superior to inferior direction) is very continuous and shows no evidence of abrupt signal changes.

3.2 | Mapping of RSNs

Figure 3 shows identified RSNs for a representative subject. Since there is no gold-standard set of networks to study rs-fMRI data, the

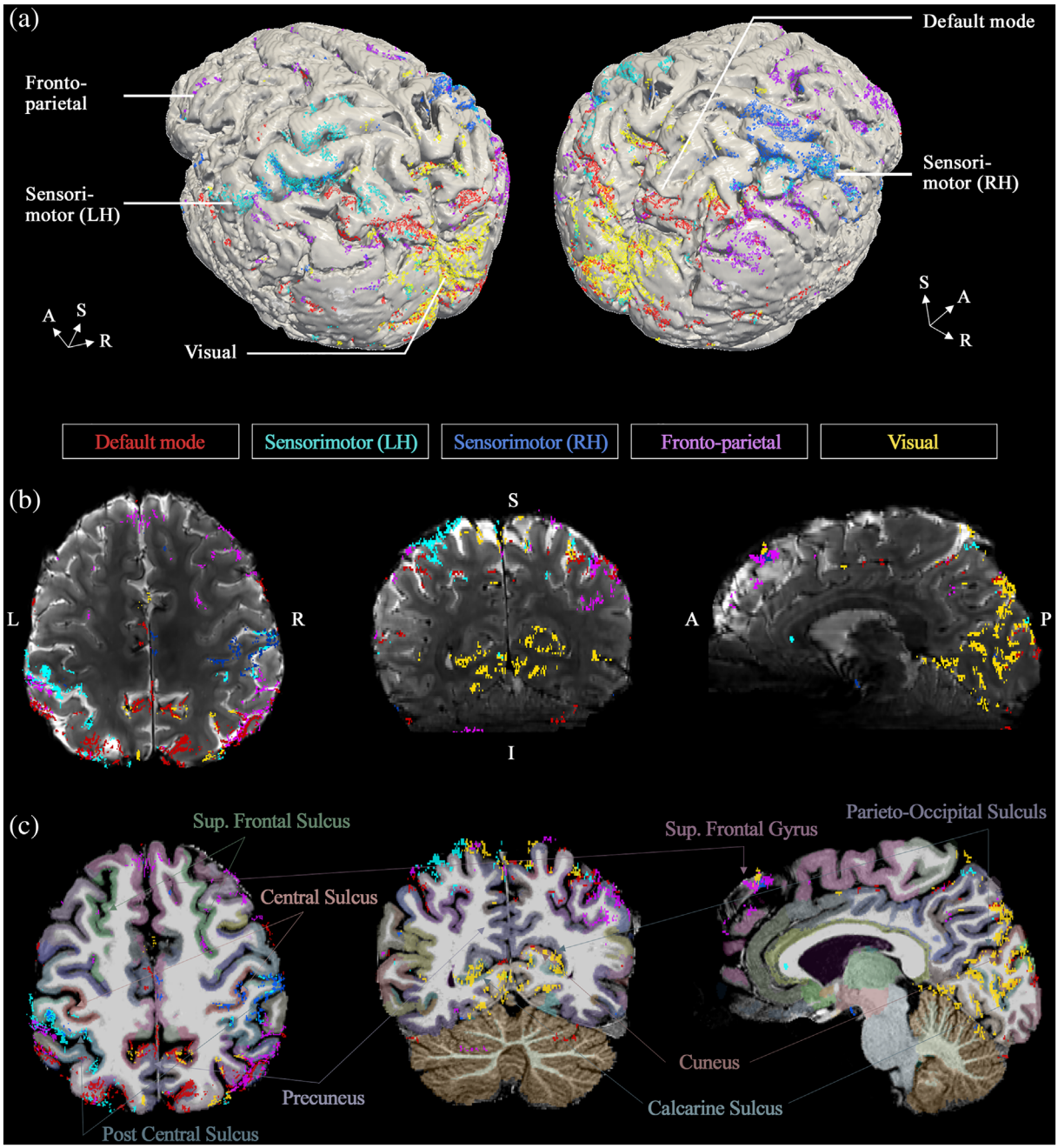

FIGURE 3 Whole-cerebrum resting-state networks (RSNs) for the half-millimetre protocol. The activated voxels were obtained with a statistical threshold (probability ≥.5). Resting-state results are shown for the following five selected networks: default mode, sensorimotor (LH), sensorimotor (RH), fronto-parietal and visual; here, LH and RH denote left hemisphere and right hemisphere, respectively. The activated voxels are shown, overlaid on (a) a 3D rendered surface of the mean image of the re-aligned functional scans, (b) three sectional slices (axial, coronal and sagittal) and (c) the anatomical scan (i.e., MP2RAGE). This figure demonstrates the performance of TR-external EPIK in terms of brain coverage (108 mm in superior–inferior direction) and the localisation of the activated voxels on the cortical ribbons (nominal spatial resolution: $0.51 \times 0.51\ mm^2$)

following five networks were selected here: default mode, sensorimotor (LH), sensorimotor (RH), fronto-parietal (executive) and the visual network, all of which were relatively common in our subjects. The activated voxels were overlaid on the 3D rendered outer cortical surface, which was generated by applying the standard SPM segmentation routine to the mean image of the re-aligned functional scans. Figure 3b shows the results presented in three different sectional views (axial, coronal and sagittal). The anatomical scan showing the same representation of the activated voxels can be seen in Figure 3c. Figure 3 clearly demonstrates that the extensive brain coverage provided by TR-external EPIK enabled the five RSNs to be simultaneously determined from a single fMRI session. In addition, the half-millimetre protocol ($0.26\ mm^3$ voxels) enabled the identification of functional voxels very locally along the cortical ribbon.

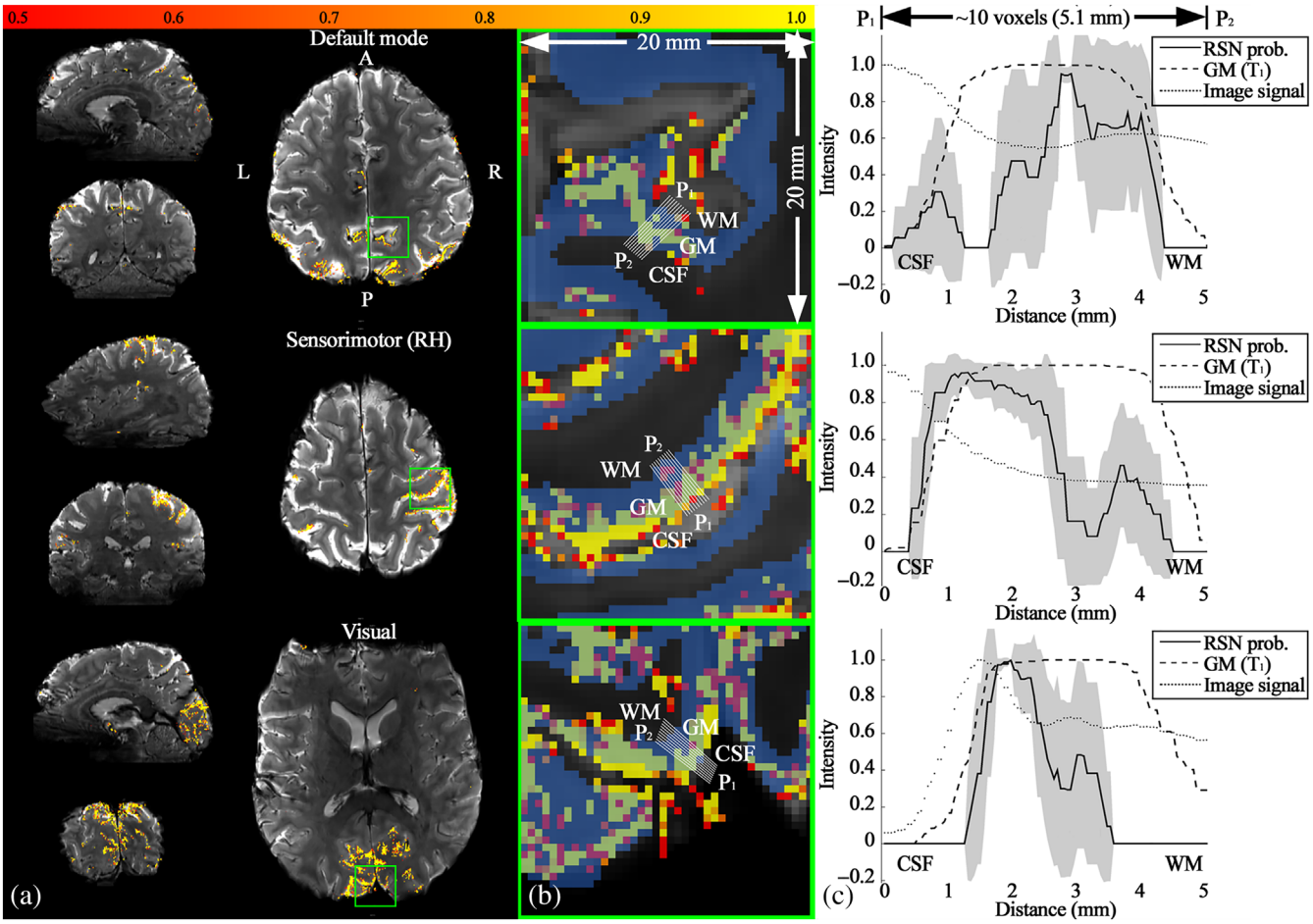

FIGURE 4 Results of the resting-state networks (RSNs) and line profiles. (a) Three RSNs (default mode, sensorimotor (RH) and visual) overlaid on their representative axial, sagittal and coronal slice locations, (b) enlarged depiction of the ROIs, marked by the green rectangles in figure a and (c) mean ± SD line profile of the network-specific probability at the 20 white lines, denoted with the points P_1 (start) and P_2 (end). The blue colour in figure b denotes grey matter (GM) regions obtained from the segmentation of the anatomical scan. In figure c, the length of each examined line is approximately 10 voxels (5.1 mm), and 100 points were sampled along its length. Here, the unit of the vertical axis represents normalised relative intensity for each of the three quantities ('RSN probability', 'GM' and 'image signal')

For a more detailed examination, three RSNs (default mode, sensorimotor (RH) and visual) are displayed separately in their representative axial, coronal and sagittal slices (Figure 4a); directly overlaid on the mean image of the re-aligned functional scans. For each network, an ROI was selected (marked with a green rectangle) and is displayed in a magnified view in Figure 4b. The size of the selected ROI is 40×40 voxels (i.e., 20×20 mm^2), and the GM regions obtained from the segmentation of the co-registered anatomical scan using FreeSurfer are depicted in blue. Here, in order to investigate the behaviour of the functional profiles around the grey matter, 20 lines, starting from 'P_1' and ending at 'P_2' and crossing the cortical ribbon, were manually defined from each enlarged depiction. The network-specific probability profiles along the lines were examined, and their mean ± SD profile is shown in Figure 4c (see the solid black line). The length of each examined line was 10 voxels (5.1 mm), and 100 points were sampled along its length. In the same figure, the signal intensity of the background image is also plotted with a black dotted line, and a gradual decrease in signal intensity can be observed from the cerebrospinal fluid (CSF) to the WM region (i.e., T_2/T_2^* contrast). The GM region obtained from the anatomical scan is also delineated here with a dashed line, which verifies that the functional activation from the three networks is mostly confined to the GM regions. The peak that is found around the pial surface in Figure 4c likely corresponds to the effect of the large-vessel contribution in the gradient-echo EPI sequences.

3.3 | RSNs from a group of subjects: reproducibility

Table 1 shows the image SNR of the acquired functional time-series data from each subject. The standard deviation of the SNR observed from each subject is shown to be very small, that is, on average, 4.29/2.07 (entire brain/GM), demonstrating that no significant SNR variation along the temporal dimension accrued during the fMRI session. Moreover, the averaged image SNR from all subjects for all

temporal scans was 251.63/231.37 (entire brain/GM), and its standard deviation across subjects was 26.64/35.57 (entire brain/GM). Notwithstanding the fact that the SNR varies between subjects, the relatively small standard deviation across subjects indicates that robust fMRI acquisition was performed throughout.

Figure 5 summarises the RSNs obtained from the 13 subjects for five well-known RSNs: auditory, default mode, sensorimotor, fronto-parietal and visual. The plot shows that although the detection pattern was different between subjects, overall, the RSNs were reliably detected, which demonstrates the robust performance of the half-millimetre protocol in the detection of RSNs.

Figure 6 shows individually displayed, activated voxels at their respective slice location for five representative subjects in the same RSN (e.g., subjects 3, 4, 5, 8 and 10 for the auditory network). The figure reveals that the identified networks had a similar activation pattern across different subjects, which demonstrates the reproducibility of mapping RSNs using TR-external EPIK. In addition, the localisation of the activated voxels along the cortical ribbon can also be verified from each subject.

The reproducibility of the detection of RSNs was further verified with the results of the second level analysis (see Figure 7). For each network, the mean group-wise activated voxels are depicted on the averaged anatomical scan. Here, the number of subjects used for the group analysis is shown in each image panel (e.g., $n = 7$ for auditory). Although the background image is blurry due to averaging, it can be seen that the RSNs were reliably detected from a group of subjects. The identified RSNs were also shown to have a good agreement with those from the reference template RSNs defined in the MNI space; that is, the spatial correlation of each RSN was highest with the same RSN from the template and lower for different RSNs (see the correlation matrix at bottom-right of Figure 7).

TABLE 1 Image SNR of the half-millimetre protocol

Subject	Entire brain/GM
1	272.88 ± 4.35/240.47 ± 4.01
2	233.83 ± 4.51/199.93 ± 1.77
3	289.65 ± 6.62/274.92 ± 3.67
4	244.25 ± 3.99/207.37 ± 2.58
5	287.95 ± 4.81/268.34 ± 1.38
6	279.82 ± 3.24/276.62 ± 1.34
7	261.40 ± 2.89/261.63 ± 1.75
8	256.55 ± 2.71/240.94 ± 1.69
9	256.70 ± 9.07/245.27 ± 1.81
10	218.67 ± 3.81/211.71 ± 2.09
11	239.45 ± 3.30/229.98 ± 1.78
12	220.99 ± 2.87/161.90 ± 1.13
13	209.00 ± 3.65/188.76 ± 1.95
Average	251.63 ± 4.29/231.37 ± 2.07

Note: For each subject, the mean ± SD across the temporal dimension (i.e., in total, 172 temporal volumes) is shown, calculated over the entire brain as well as the GM region only. The last row shows the average of the computed SNR values from all subjects. The standard deviation of SNR across the 13 subjects was computed as 26.64 and 35.57 for the entire brain and the GM, respectively.

3.4 | Imaging performance of the half-millimetre protocol

Figure 8 shows the imaging parameters employed in our present work in comparison to those in previous submillimetre-resolution fMRI studies. As shown in Figure 8a, TR-external EPIK has the highest in-

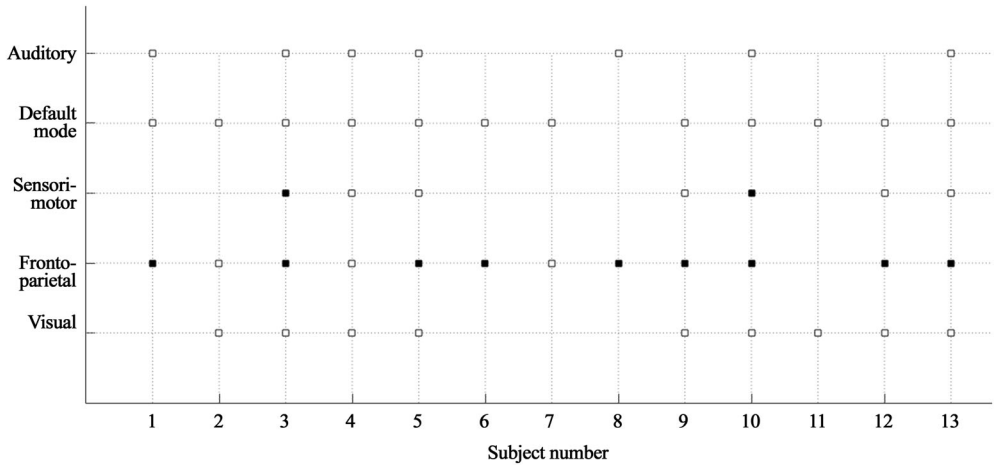

FIGURE 5 A grid plot of resting-state networks (RSNs) with respect to the 13 subjects. For five well-known functional networks (auditory, default mode, sensorimotor, fronto-parietal and visual), the RSNs detected in each subject are marked with a square. The solid squares in the somatosensory and the parietal networks present the case when the activation was found in both hemispheres (i.e., bi-hemispheric activation); lateralised activation (either in the left or in the right hemisphere) is depicted by the open squares. This figure demonstrates that overall, the RSNs were reliably detected

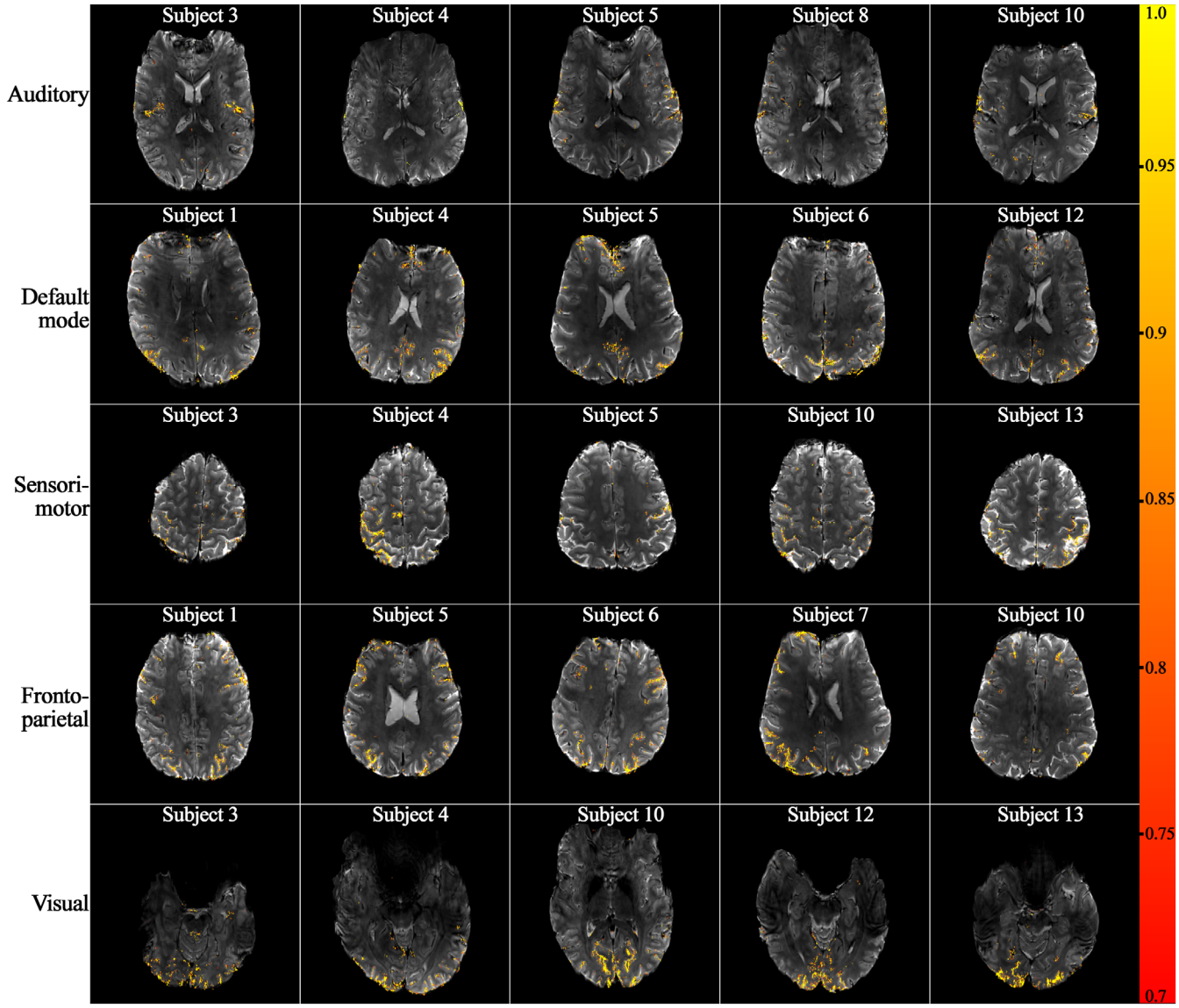

FIGURE 6 Reproducibility in the detection of RSNs. For each of the five resting-state networks (RSNs; auditory, default mode, sensorimotor, fronto-parietal and visual), the activated voxels from five representative subjects are shown, directly overlaid on the functional scan. A similar activation pattern can be observed over all subjects for each network, demonstrating the reproducibility of functional mapping

plane spatial resolution (0.51 mm) compared to prior publications. Importantly, the spatial resolution was achieved with a sufficiently large in-plane FOV (210 mm), which can cover an entire normal, adult-sized brain sliced in any orientation (see Figure 8b). In comparison, the normalised in-plane FOV provided in most prior studies was smaller than 150 mm, indicating that only a particular slice location and rotation would allow the brain to be entirely encompassed within the in-plane FOV. To facilitate a robust SNR for a group study, the employed slice thickness in TR-external EPIK (1 mm) was larger than its in-plane voxel size. However, Figure 8c shows that there are also submillimetre-resolution fMRI studies performed with a non-isovoxel size where the slice thickness reaches as high as 1.8 mm. The results of normalised slice throughput showed that it was smaller than 50 for most prior cases (see Figure 8d). TR-external EPIK gave the second largest normalised slice throughput, with the method proposed by Kay et al. giving the largest. However, the comparatively smaller slice throughput in TR-external EPIK can be explained as being due to the significantly bigger in-plane matrix size of TR-external EPIK (408×408) when compared to that of Kay et al. (2019) (200×162). Figure 8e,f also shows that TR-external EPIK gives the third minimum voxel volume (0.26 mm^3) and the largest number of voxels per temporal volume (17.98 M). In TR-external EPIK, the spatial resolution and the slice throughput were achieved under a typical TE and volumetric TR setting. That is, the values from our study (22 ms/3500 ms) are shown to be within the range of values provided in other literature, and even longer TEs and TRs can be found depending on the application (see Figure 8g,h). More detailed imaging parameters of the prior studies and the technical

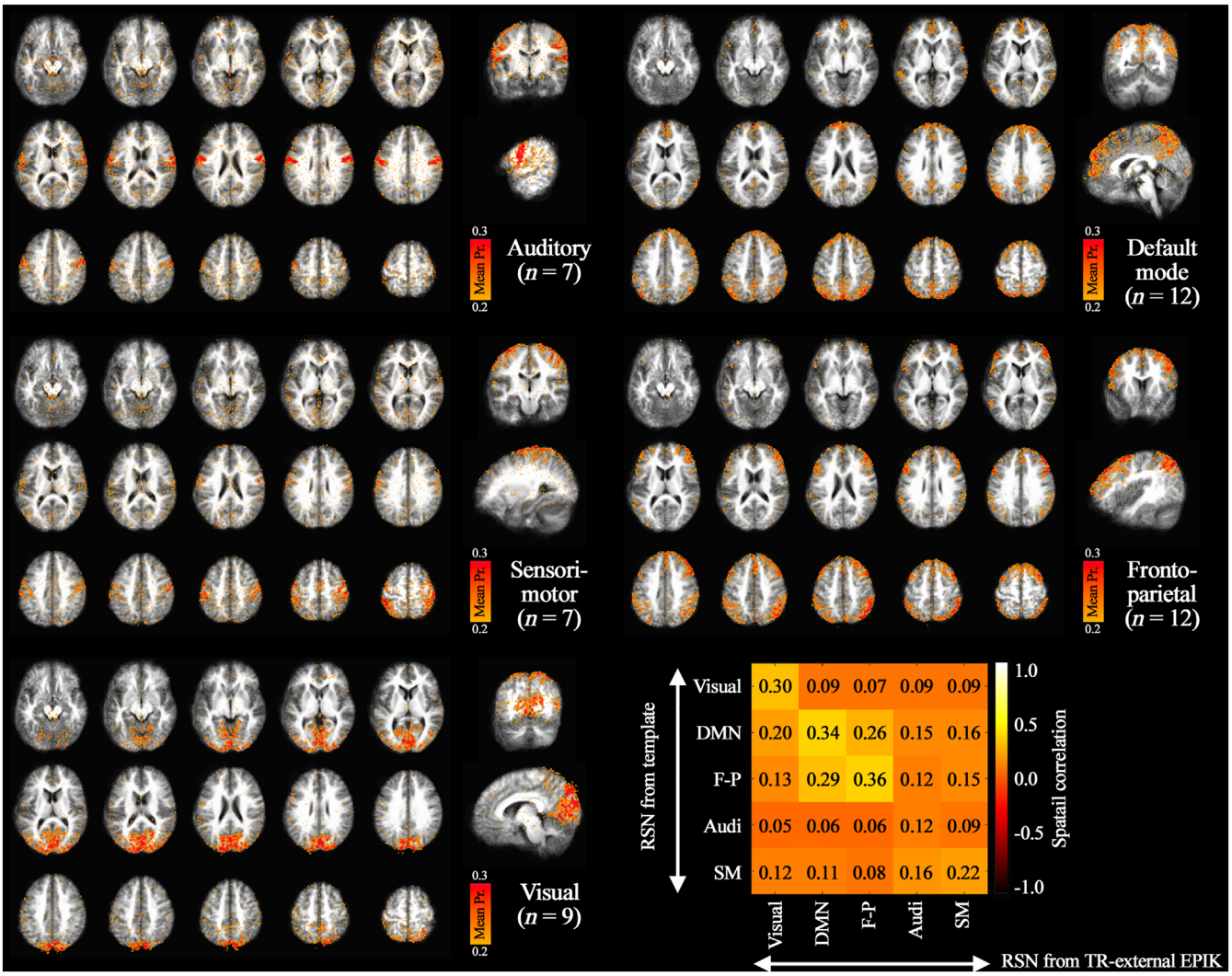

FIGURE 7 Results of second level analysis of the half-millimetre protocol. The group-wise activated voxels from each resting-state network (RSN) are shown on the averaged anatomical scan. The figure demonstrates the reliable detection of RSNs for a group of subjects. The image panel on the bottom right shows the spatial correlation between the identified RSNs in this work and those from the template RSNs defined in the Montreal Neurological Institute (MNI) space

performance of TR-external EPIK can be found in Supporting Information (Tables S1, S2 and Figure S5).

3.5 | RSN results for an isovoxel protocol

The application of TR-external EPIK for rs-fMRI was also demonstrated with an isovoxel protocol ($0.63 \times 0.63 \times 0.63$ mm^3) for the same group of subjects as employed in the half-millimetre protocol. Figure 9 shows results for the same five RSNs as depicted in the half-millimetre protocol case. The same second-level analysis and spatial correlation computation were also carried out (see Figure 10). These results also show a high mapping fidelity onto the cortical ribbon and robustness in detecting the same RSNs as the half-millimetre case. Verification of TR-external EPIK for other submillimetre isovoxel sizes is given in Supporting Information (see Figure S6).

4 | DISCUSSION

4.1 | TR-external EPIK for high-resolution fMRI

This work demonstrates the ability of the TR-external EPIK mapping technique to achieve a half-millimetre in-plane pixel size and enable the acquisition of whole-cerebrum, resting-state functional signals at 7T. The technique was developed based on EPIK and a TR-external EPI phase correction.

The feasibility of using EPIK for fMRI has been verified in several previous publications (Yun et al., 2013; Yun, Shah, et al., 2019; Yun & Shah, 2017). The features of EPIK and the rationale for its use in the fMRI conducted in these works are described in detail in the Supporting Information (see Section 5.1). An explanation is provided for the following five topics: (1) Comparison of fMRI results to the community-standard method, EPI, (2) Temporal stability and the importance of keyhole-region sampling, (3) Spatial resolution and point spread

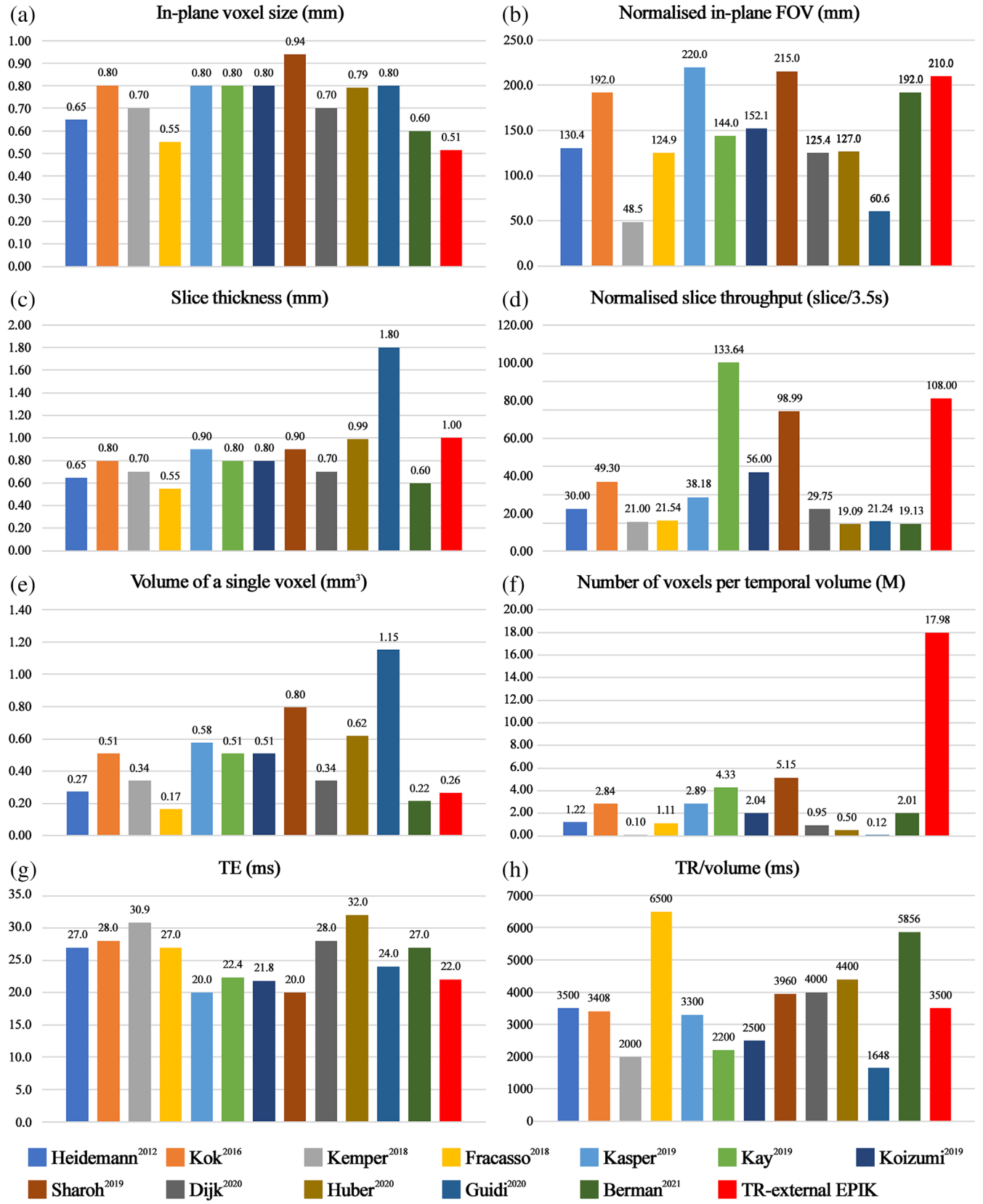

FIGURE 8 Imaging performance of TR-external EPIK in comparison to other submillimetre-resolution studies. The eight bar charts above show a comparison of the imaging parameters used in the current study and 12 previous submillimetre fMRI studies performed at 7T. The parameters compared were: (a) in-plane voxel size (mm), (b) normalised in-plane FOV (mm), (c) slice thickness (mm), (d) normalised slice throughput (slice/3.5 s), (e) volume of a single voxel (mm^3), (f) number of voxels per temporal volume (M), (g) TE (ms) and (h) TR/volume (ms)

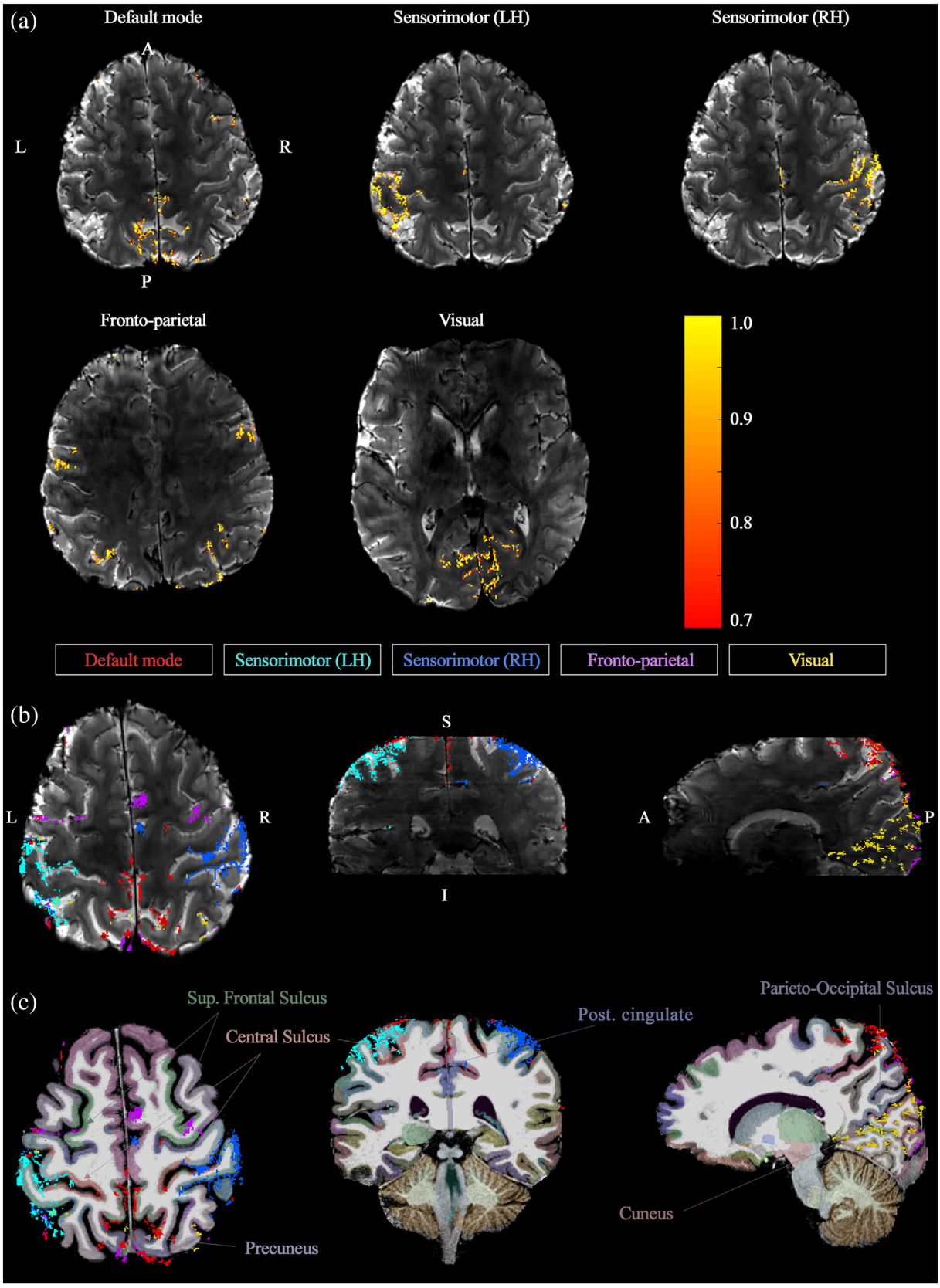

FIGURE 9 Results of resting-state networks (RSNs) obtained with the isovoxel protocol. The five identified RSNs (default mode, sensorimotor (LH), sensorimotor (RH), fronto-parietal and visual) are shown, overlaid on (a) their representative axial slice locations, (b) three sections slices (axial, coronal and sagittal) and (c) the anatomical scan (i.e., MP2RAGE)

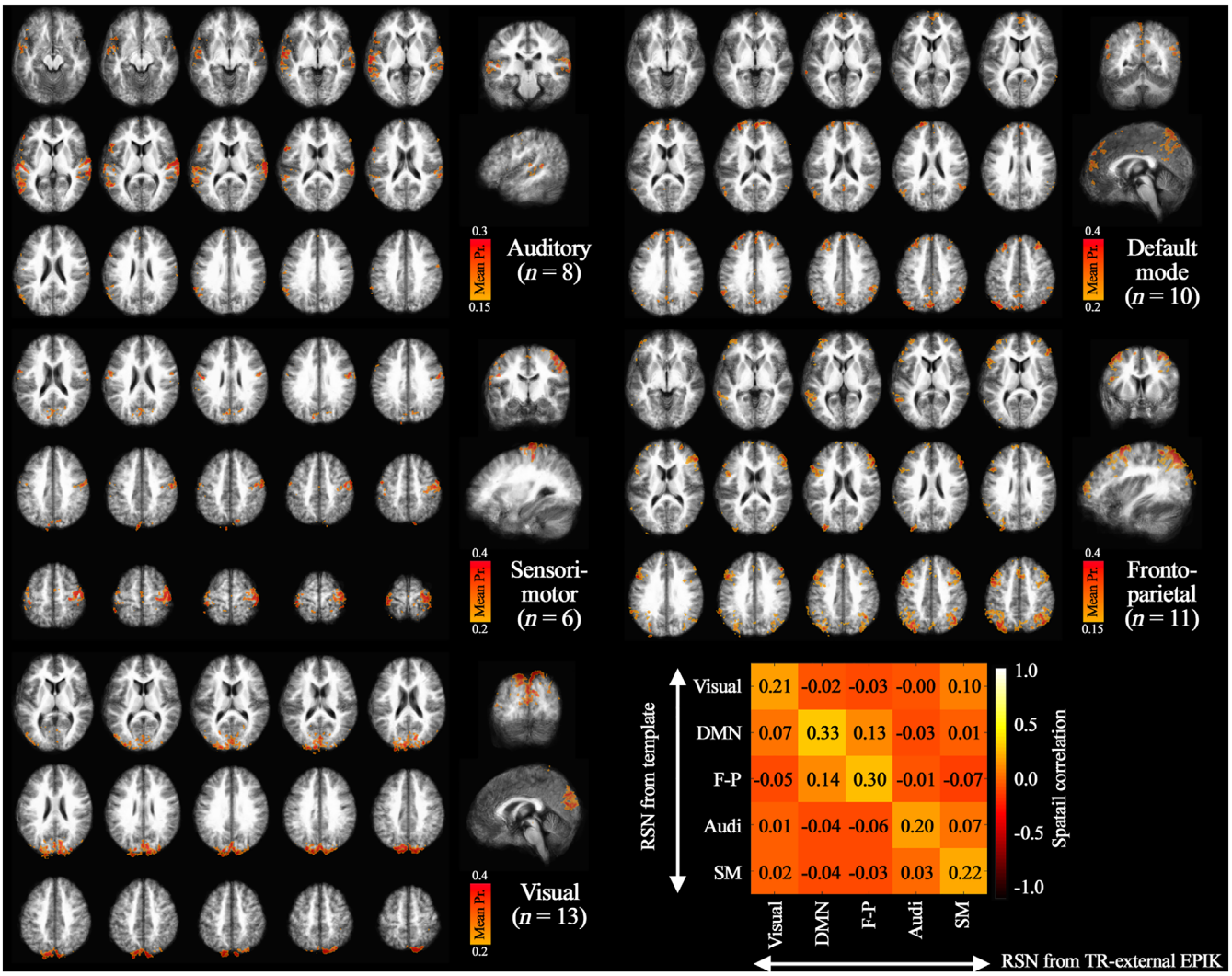

FIGURE 10 Results of the second level analysis of the isovoxel protocol. Similar to the half-millimetre protocol case, the results demonstrate the reliable detection of resting-state networks (RSNs) for a group of subjects and show good agreement with the template RSNs

function (PSF), (4) Temporal detectability of functional signals and 5) Limitations of EPIK. The TR-external implementation of the navigator echoes shortens the minimum possible TE in the main imaging sub-loop enabling higher resolution fMRI (Yun & Shah, 2020) compared to the TR-internal implementation scheme (Heid, 1997; Wong, 1992). In this work, this benefit, in combination with EPIK, allowed an in-plane matrix size of 408 × 408 (0.51 × 0.51 mm^2) with a TE of 22 ms and a FOV of 210 × 210 mm^2. Importantly, this in-plane FOV combined with the acquisition of 108 slices (1 mm thick) is large enough to cover an entire typical human cerebrum sliced in any direction.

Although there have been numerous submillimetre-resolution fMRI studies, the voxel size provided in most previous methods was achieved using a considerably smaller matrix size (<200 × 200) and a smaller FOV (<200 × 200 mm^2) than TR-external EPIK, meaning that only a part of the brain was imaged. Moreover, the slice throughput determining the brain coverage was also substantially smaller in the previous works. Due to the above technical limitations, rs-fMRI has not previously been performed with the spatial resolution and brain coverage demonstrated here. In this work, a relatively long TR (3.5 s) was employed to record the rs-fMRI signals. However, since rs-fMRI focuses on low-frequency fluctuations (<0.1 Hz), conventional data analyses require a TR of 5 s to cope with the Nyquist sampling of the upper limit (Berman et al., 2021). Accordingly, the use of a long TR for rs-fMRI has also been demonstrated in previous publications: TR of 3960, 5000 and 5856 ms (Barry et al., 2021; Berman et al., 2021; Sharoh et al., 2019). Depending on the method selected from the literature, it may be possible to achieve an increased spatial resolution or larger slice coverage by a protocol adjustment. Despite the difficulty of performing a fair comparison between different methods under the given imaging conditions, the comparison results show that the TR-external method offers clear improvements.

4.2 | Spatial resolution of TR-external EPIK

The relatively long readout in EPI-based sequences can deleteriously affect the spatial resolution of the reconstructed image. That notwithstanding,

the PSF analysis performed both in our prior (Yun et al., 2013; Yun & Shah, 2017; Yun, Shah, et al., 2019) and current work (Figure S5b) shows that EPIK has a sharper PSF shape and better spatial resolution than EPI when all other parameters are held constant. This work employed a relatively large partial Fourier acceleration factor (PF of 5/8) for the half-millimetre protocol. However, results from the PSF simulation (Figure S5d) showed that the spatial resolution is determined not only by the partial Fourier factor, but also by the imaging matrix size, that is, the number of actually sampled points = partial Fourier factor × imaging matrix size. Therefore, despite the high partial Fourier factor, the relatively large matrix size (408 × 408) in our work substantially increases the number of sampled points, subsequently contributing to enhanced spatial resolution. It is noted that several previous submillimetre-resolution fMRI studies (Feinberg et al., 2018; Kashyap et al., 2021; Maass et al., 2015) employing a PF of 5/8 also used a relatively large matrix size (e.g., 213 × 213 and 256 × 256) which was, however, much smaller than that of the TR-external EPIK sequence used here.

The spatial resolution of TR-external EPIK was demonstrated for the identification of mesoscale anatomical structures such as small cerebral vessels or a dark stripe, which is located at approximately 50% of the cortical depth in discrete regions throughout the brain. Within the calcarine sulcus, this stripe resembles the stria of Gennari, which is a heavily myelinated tangential band at 60% of the cortical depth (Vogt & Vogt, 1919) and is only visible in high-resolution structural MRI (Clare & Bridge, 2005; Eickhoff et al., 2005; Walters et al., 2007). Although the stria of Gennari is a feature unique to the primary visual cortex (Zilles et al., 2015), we also detected comparable stripes in the anterior wall of the postcentral gyrus (primary somatosensory area 3), on the Heschl gyrus (primary auditory cortex) and in the parietal operculum (secondary somatosensory cortex). Furthermore, of these areas, only the primary somatosensory cortex is characterised by the presence of two clearly identifiable Baillarger stripes (myeloarchitectonic layer 4 or 5b), of which, the inner one is more densely myelinated than the outer one (Zilles et al., 2015). A common feature of all areas containing a dark stripe is the presence of a prominent and densely packed inner granular layer. Therefore, we have interpreted the stripe as being cytoarchitectonic layer IV and not myeloarchitectonic layer 4 or 5b. It is important to note that these features were visible in fMRI images, which are primarily intended to depict function and not to demonstrate anatomical features.

This work employed a relatively small acceleration combination for parallel imaging and multi-band techniques (i.e., 3 × 3), which ensured reliable image reconstruction without significant intra-slice aliasing or inter-slice leakage artefacts (McNabb et al., 2020). However, further improvements in spatiotemporal resolution may also be possible in TR-external EPIK by means of a higher acceleration combination, such as 4 × 4 or 2 × 5, as demonstrated in previous works (Moeller et al., 2010; Vu et al., 2017).

4.3 | Resting-state networks

For application purposes, the half-millimetre protocol was verified with rs-fMRI on 13 healthy subjects. The SNR results showed that the functional images were reliably acquired without any significant SNR variation during each fMRI session and the inter-subject variation was also very small. The reproducibility in the detection of RSNs was verified with a group analysis performed in both subject-specific and common-template space. Furthermore, network-specific probability profiles additionally showed signal variation within the cortical regions, indicating that TR-external EPIK may be useful for cortical depth-dependent functional studies.

The slice thickness (1.0 mm) used in the half-millimetre protocol was selected to provide a robust SNR for a group of subjects and subsequently check the reproducibility of TR-external EPIK. It is noted that several previous submillimetre-resolution fMRI studies employed non-isovoxel sizes to identify cortical depth-dependent activation from an individual subject-based measurement. Depending on the study's purpose, a more optimal half-millimetre protocol with a smaller slice thickness or an isovoxel size may be possible with TR-external EPIK. This work also demonstrated the use of an isovoxel size ($0.63 \times 0.63 \times 0.63\ mm^3$) where the reliable detection of RSNs with a high mapping fidelity was shown.

4.4 | Non-BOLD contrasts

In order to overcome the relatively low spatial specificity to neuronal activation in gradient-echo (GE) BOLD, several non-BOLD contrasts have previously been demonstrated using cerebral blood flow (e.g., ASL), cerebral blood volume (e.g., VASO) or cerebral metabolic rate of oxygen (e.g., calibrated BOLD)(Borogovac & Asllani, 2012; Huber et al., 2017 and 2019; Germuska & Wise, 2019). Although the non-BOLD contrasts offer improved spatial specificity and functional quantification, they have relatively low sensitivity compared to GE-BOLD contrast (10%–20% for ASL, 40%–60% for VASO and 5%–15% for calibrated BOLD) (Huber et al., 2019), making their use in submillimetre-resolution fMRI challenging. Furthermore, the underlying mechanisms of each contrast (e.g., labelling, blood nulling or reach of functional steady-state) usually requires a much longer TR than the GE-BOLD method, which may provide limited brain coverage for a given TR. For these reasons, fMRI methods with GE-BOLD contrasts are still widely used in submillimetre-resolution fMRI. Several approaches have been used to reduce the large-vessel BOLD effect in GE-BOLD by applying a correction method or replacing it with spin-echo BOLD. In this work, the correction method (Curtis et al., 2014; Menon, 2002) was applied to reduce the large-vessel effect. However, as our earlier work verified the use of spin-echo EPIK for detecting haemodynamic signals in a perfusion study (Shah et al., 2019), it is expected that spin-echo TR-external EPIK can also be systematically configured to give the same high-resolution advantage as well as increased spatial specificity.

4.5 | Functional resolution

One of the main challenges of interpreting high-resolution fMRI relates to the complexity of the neural hemodynamic responses and

the heterogeneous vascular network topology of the cerebral cortex (Duvernoy et al., 1981; Havlicek & Uludag, 2020). Neuronal activity is coupled to an increase in the cerebral metabolic rate of oxygen, which, under conditions of normal neuro-vascular coupling, triggers a local increase in the cerebral blood flow and volume that can be detected with fMRI sequences. However, the specific temporal dynamics of the vascular responses (i.e., the hemodynamic response function) can alter depending on the vascular environment, for example, across different cortical layers (Heinzle et al., 2016; Tian et al., 2010). In particular, the heterogeneously distributed cerebral veins and venules (large pial veins running tangentially to the cortex and ascending venules draining blood from deep cortical layers towards the surface) introduce a bias in the fMRI signal and is especially prevalent in GE-studies where the contribution of the macrovasculature is considerably higher. Moreover, the varying capillary density across the cortical depth further conditions the actual spatial resolution of functional responses. Simulation studies have demonstrated an enhanced specificity of the fMRI signal towards the microvasculature at higher fields using short TEs (Pflugfelder et al., 2011). Additionally, several works have estimated the PSF of the hemodynamic responses linked to neuronal activity, which would represent the minimum space unit that could be resolved with fMRI contrast. This ultimate resolution was estimated to be 0.1 mm in an optical study of the cerebral blood volume in mice (Vazquez et al., 2014), 0.86 mm for spin-echo BOLD fMRI and 0.99 mm for GE-BOLD fMRI in a human study of ocular dominance columns (Chaimow et al., 2018). Taking into account the unavoidable presence of physiological motion and the resultant blurring in human fMRI, the true haemodynamic PSF is probably narrower than the PSF in the presence of physiological motion, which in turn results in a higher putative functional resolution. Notwithstanding the controversial definition of the ultimate functional spatial resolution, the fact that published, experimental submillimetre fMRI studies have detected distinct signals originating in highly segregated cortical units, such as cytoarchitectonically-defined layers (e.g., cortical depth-specific activation upon engagement of a finger in a sensory or a motor task [Huber et al., 2017]), strongly supports the ambition of acquiring and analysing functional data with submillimetre-resolution as high as provided here by TR-external EPIK ($0.51 \times 0.51 \times 1.0$ mm^3; $0.63 \times 0.63 \times 0.63$ mm^3).

4.6 | Potential use of TR-external EPIK

In high-resolution fMRI studies, an errorless co-registration between functional and anatomical scans is often required to aid a better depiction of functional signals. A recent work has presented a method that effectively reduces the co-registration errors stemming from the use of different imaging sequences for functional and anatomical scans by using the same base sequence for both scans (van der Zwaag et al., 2018). The current work showed that our TR-external EPIK protocol enabled the detection of an activation profile within the cortical regions, and a more detailed analysis relating to the depth-dependent activation will be the focus of future studies. Furthermore, the spin-echo configuration of TR-external EPIK will also be explored, and a similar high-resolution advantage and spatial specificity are expected. A comparison of SE-BOLD TR-external EPIK with non-BOLD methods will also be investigated in potential future work.

ACKNOWLEDGMENT

The authors would like to thank the volunteers for their participation in this work and Claire Rick for English proofreading. Further, open access publication was funded by the Deutsche Forschungsgemeinschaft (DFG, German Research Foundation) - 491111487. Open access funding enabled and organized by Projekt DEAL.

CONFLICT OF INTEREST

The authors declare no potential conflict of interest.

DATA AVAILABILITY STATEMENT

The original in vivo data from 13 subjects can be shared by submitting a request to the corresponding author (N. Jon Shah: n.j.shah@fz-juelich.de) under a formal data-sharing agreement. The general protection of personal data and privacy policy, declared by the Council of Europe (https://www.coe.int/en/web/portal/personal-data-protection-and-privacy), applies to health-related data (CM/Rec(2019)2). The protection of in vivo data or metadata derived from the original data is further described by the corresponding ethics/internal administrating documents. The sharing is based on the consent of the subject whose data are to be shared; these subjects will be informed beforehand.

ORCID

Seong Dae Yun https://orcid.org/0000-0001-7398-1899
Patricia Pais-Roldán https://orcid.org/0000-0002-9381-3048
Nicola Palomero-Gallagher https://orcid.org/0000-0003-4463-8578
N. Jon Shah https://orcid.org/0000-0002-8151-6169

REFERENCES

Adhikari, B. M., Hong, L. E., Sampath, H., Chiappelli, J., Jahanshad, N., Thompson, P. M., Rowland, L. M., Calhoun, V. D., Du, X., Chen, S., & Kochunov, P. (2019). Functional network connectivity impairments and core cognitive deficits in schizophrenia. *Human Brain Mapping*, *40*(16), 4593–4605. https://doi.org/10.1002/hbm.24723

Barry, R. L., Babu, S., Anteraper, S. A., Triantafyllou, C., Keil, B., Rowe, O. E., & Atassi, N. (2021). Ultra-high field (7T) functional magnetic resonance imaging in amyotrophic lateral sclerosis: a pilot study. *NeuroImage: Clinical*, *30*, 102648. https://doi.org/10.1016/j.nicl.2021.102648

Berman, A. J. L., Grissom, W. A., Witzel, T., Nasr, S., Park, D. J., Setsompop, K., & Polimeni, J. R. (2021). Ultra-high spatial resolution BOLD fMRI in humans using combined segmented-accelerated VFA-FLEET with a recursive RF pulse design. *Magnetic Resonance in Medicine*, *85*(1), 120–139. https://doi.org/10.1002/mrm.28415

Biswal, B., Hudetz, A. G., Yetkin, F. Z., Haughton, V. M., & Hyde, J. S. (1997). Hypercapnia reversibly suppresses low-frequency fluctuations in the human motor cortex during rest using echo-planar MRI. *Journal of Cerebral Blood Flow and Metabolism*, *17*(3), 301–308. https://doi.org/10.1097/00004647-199703000-00007

Biswal, B., Yetkin, F. Z., Haughton, V. M., & Hyde, J. S. (1995). Functional connectivity in the motor cortex of resting human brain using echo-planar MRI. *Magnetic Resonance in Medicine*, *34*(4), 537–541. https://doi.org/10.1002/mrm.1910340409

Borogovac, A., & Asllani, I. (2012). Arterial spin labeling (ASL) fMRI: Advantages, theoretical constrains and experimental challenges in neurosciences. *International Journal of Biomedical Imaging*, *2012*, 818456. https://doi.org/10.1155/2012/818456

Caldeira, L. L., Yun, S. D., da Silva, N. A., Filss, C., & Shah, N. J. (2019). Dynamic susceptibility contrast parametric imaging using accelerated dual-contrast echo planar imaging with keyhole. *Journal of Magnetic Resonance Imaging*, *50*(2), 628–640. https://doi.org/10.1002/jmri.26639

Chai, Y. H., Li, L. Q., Huber, L., Poser, B. A., & Bandettini, P. A. (2020). Integrated VASO and perfusion contrast: A new tool for laminar functional MRI. *NeuroImage*, *207*, 116358. https://doi.org/10.1016/j.neuroimage.2019.116358

Chaimow, D., Yacoub, E., Ugurbil, K., & Shmuel, A. (2018). Spatial specificity of the functional MRI blood oxygenation response relative to neuronal activity. *NeuroImage*, *164*, 32–47. https://doi.org/10.1016/j.neuroimage.2017.08.077

Clare, S., & Bridge, H. (2005). Methodological issues relating to in vivo cortical myelography using MRI. *Human Brain Mapping*, *26*(4), 240–250. https://doi.org/10.1002/hbm.20162

Curtis, A. T., Hutchison, R. M., & Menon, R. S. (2014). Phase based venous suppression in resting-state BOLD GE-fMRI. *NeuroImage*, *100*, 51–59. https://doi.org/10.1016/j.neuroimage.2014.05.079

Duvernoy, H. M., Delon, S., & Vannson, J. L. (1981). Cortical blood-vessels of the human-brain. *Brain Research Bulletin*, *7*(5), 519–579. https://doi.org/10.1016/0361-9230(81)90007-1

Eickhoff, S., Walters, N. B., Schleicher, A., Kril, J., Egan, G. F., Zilles, K., Watson, J. D. G., & Amunts, K. (2005). High-resolution MRI reflects myeloarchitecture and cytoarchitecture of human cerebral cortex. *Human Brain Mapping*, *24*(3), 206–215. https://doi.org/10.1002/hbm.20082

Fang, Z., Van Le, N., Choy, M., & Lee, J. H. (2016). High spatial resolution compressed sensing (HSPARSE) functional MRI. *Magnetic Resonance in Medicine*, *76*(2), 440–455. https://doi.org/10.1002/mrm.25854

Feinberg, D. A., Vu, A. T., & Beckett, A. (2018). Pushing the limits of ultra-high resolution human brain imaging with SMS-EPI demonstrated for columnar level fMRI. *NeuroImage*, *164*, 155–163. https://doi.org/10.1016/j.neuroimage.2017.02.020

Fracasso, A., Luijten, P. R., Dumoulin, S. O., & Petridou, N. (2018). Laminar imaging of positive and negative BOLD in human visual cortex at 7 T. *NeuroImage*, *164*, 100–111. https://doi.org/10.1016/j.neuroimage.2017.02.038

Germuska, M., & Wise, R. G. (2019). Calibrated fMRI for mapping absolute CMRO2: Practicalities and prospects. *NeuroImage*, *187*, 145–153. https://doi.org/10.1016/j.neuroimage.2018.03.068

Griswold, M. A., Jakob, P. M., Heidemann, R. M., Nittka, M., Jellus, V., Wang, J. M., Kiefer, B., & Haase, A. (2002). Generalized autocalibrating partially parallel acquisitions (GRAPPA). *Magnetic Resonance in Medicine*, *47*(6), 1202–1210. https://doi.org/10.1002/mrm.10171

Guidi, M., Huber, L., Lampe, L., Gauthier, C. J., & Moller, H. E. (2016). Lamina-dependent calibrated BOLD response in human primary motor cortex. *NeuroImage*, *141*, 250–261. https://doi.org/10.1016/j.neuroimage.2016.06.030

Guidi, M., Huber, L., Lampe, L., Merola, A., Ihle, K., & Moller, H. E. (2020). Cortical laminar resting-state signal fluctuations scale with the hypercapnic blood oxygenation level-dependent response. *Human Brain Mapping*, *41*(8), 2014–2027. https://doi.org/10.1002/hbm.24926

Havlicek, M., & Uludag, K. (2020). A dynamical model of the laminar BOLD response. *NeuroImage*, *204*, 116209. https://doi.org/10.1016/j.neuroimage.2019.116209

Heid, O. (1997). Robust EPI phase correction. *Paper presented at the ISMRM*, Vancouver, Canada.

Heidemann, R. M., Ivanov, D., Trampel, R., Fasano, F., Meyer, H., Pfeuffer, J., & Turner, R. (2012). Isotropic submillimeter fMRI in the human brain at 7 T: Combining reduced field-of-view imaging and partially parallel acquisitions. *Magnetic Resonance in Medicine*, *68*(5), 1506–1516. https://doi.org/10.1002/mrm.24156

Heine, L., Soddu, A., Gomez, F., Vanhaudenhuyse, A., Tshibanda, L., Thonnard, M., Charland-Verville, V., Kirsch, M., Laureys, S., & Demertzi, A. (2012). Resting state networks and consciousness: Alterations of multiple resting state network connectivity in physiological, pharmacological, and pathological consciousness states. *Frontiers in Psychology*, *3*, 295. https://doi.org/10.3389/fpsyg.2012.00295

Heinzle, J., Koopmans, P. J., den Ouden, H. E. M., Raman, S., & Stephan, K. E. (2016). A hemodynamic model for layered BOLD signals. *NeuroImage*, *125*, 556–570. https://doi.org/10.1016/j.neuroimage.2015.10.025

Huber, L., Finn, E. S., Handwerker, D. A., Bonstrup, M., Glen, D. R., Kashyap, S., Ivanov, D., Petridou, N., Marrett, S., Goense, J., Poser, B. A., & Bandettini, P. A. (2020). Sub-millimeter fMRI reveals multiple topographical digit representations that form action maps in human motor cortex. *NeuroImage*, *208*, 116463. https://doi.org/10.1016/j.neuroimage.2019.116463

Huber, L., Goense, J., Kennerley, A. J., Trampel, R., Guidi, M., Reimer, E., Ivanov, D., Neef, N., Gauthier, C. J., Turner, R., & Moller, H. E. (2015). Cortical lamina-dependent blood volume changes in human brain at 7 T. *NeuroImage*, *107*, 23–33. https://doi.org/10.1016/j.neuroimage.2014.11.046

Huber, L., Handwerker, D. A., Jangraw, D. C., Chen, G., Hall, A., Stuber, C., Gonzalez-Castillo, J., Ivanov, D., Marrett, S., Guidi, M., Goense, J., Poser, B. A., & Bandettini, P. A. (2017). High-resolution CBV-fMRI allows mapping of laminar activity and connectivity of cortical input and output in human M1. *Neuron*, *96*(6), 1253. https://doi.org/10.1016/j.neuron.2017.11.005

Huber, L., Uludag, K., & Moller, H. E. (2019). Non-BOLD contrast for laminar fMRI in humans: CBF, CBV, and CMRO2. *NeuroImage*, *197*, 742–760. https://doi.org/10.1016/j.neuroimage.2017.07.041

Jiang, Y., Pais, P., Pohmann, R., & Yu, X. (2018). High resolution single-vessel fMRI with the radial encoding method. *Paper presented at the ISMRM*. Paris, France.

Kashyap, S., Ivanov, D., Havlicek, M., Sengupta, S., Poser, B. A., & Uludag, K. (2018). Resolving laminar activation in human V1 using ultra-high spatial resolution fMRI at 7T. *Scientific Reports*, *8*, 17063. https://doi.org/10.1038/s41598-018-35333-3

Kashyap, S., Ivanov, D., Havlicek, M., Huber, L., Poser, B. A., & Uludağ, K. (2021). Sub-millimetre resolution laminar fMRI using Arterial Spin Labelling in humans at 7 T. *PLOS ONE*, *16*(4), e0250504. https://doi.org/10.1371/journal.pone.0250504

Kasper, L., Engel, M., Heinzle, J., Mueller-Schrader, M., Reber, J., Schmid, T., Barmet, C., Wilm, B. J., Stephan, K. E., Pruessmann, K. P. (2019). Advances in spiral fMRI: A high-resolution study with single-shot acquisition. *bioRxiv*, 842179. doi:https://doi.org/10.1101/842179

Kay, K., Jamison, K. W., Vizioli, L., Zhang, R., Margalit, E., & Ugurbil, K. (2019). A critical assessment of data quality and venous effects in sub-millimeter fMRI. *NeuroImage*, *189*, 847–869. https://doi.org/10.1016/j.neuroimage.2019.02.006

Kemper, V. G., De Martino, F., Emmerling, T. C., Yacoub, E., & Goebel, R. (2018). High resolution data analysis strategies for mesoscale human functional MRI at 7 and 9.4T. *NeuroImage*, *164*, 48–58. https://doi.org/10.1016/j.neuroimage.2017.03.058

Koizumi, A., Zhan, M., Ban, H., Kida, I., De Martino, F., Vaessen, M. J., de Gelder, B., & Amano, K. (2019). Threat anticipation in pulvinar and in superficial layers of primary visual cortex (V1). Evidence from layer-specific ultra-high field 7T fMRI. *eNeuro*, *6*(6), ENEURO.0429. https://doi.org/10.1523/ENEURO.0429-19.2019

Kok, P., Bains, L. J., van Mourik, T., Norris, D. G., & de Lange, F. P. (2016). Selective activation of the deep layers of the human primary visual

cortex by top-down feedback. *Current Biology*, *26*(3), 371–376. https://doi.org/10.1016/j.cub.2015.12.038

Larkman, D. J., Hajnal, J. V., Herlihy, A. H., Coutts, G. A., Young, I. R., & Ehnholm, G. (2001). Use of multicoil arrays for separation of signal from multiple slices simultaneously excited. *Journal of Magnetic Resonance Imaging*, *13*(2), 313–317.

Maass, A., Berron, D., Libby, L. A., Ranganath, C., & Düzel, E. (2015). Functional subregions of the human entorhinal cortex. *eLife*, *4*. https://doi.org/10.7554/elife.06426

Mansfield, P. (1977). Multi-planar image formation using NMR spin echoes. *Journal of Physics C: Solid State Physics*, *10*(3), L55–L58. https://doi.org/10.1088/0022-3719/10/3/004

McNabb, C. B., Lindner, M., Shen, S., Burgess, L. G., Murayama, K., & Johnstone, T. (2020). Inter-slice leakage and intra-slice aliasing in simultaneous multi-slice echo-planar images. *Brain Structure & Function*, *225*(3), 1153–1158. https://doi.org/10.1007/s00429-020-02053-2

Menon, R. S. (2002). Postacquisition suppression of large-vessel BOLD signals in high-resolution fMRI. *Magnetic Resonance in Medicine*, *47*(1), 1–9. https://doi.org/10.1002/mrm.10041

Moeller, S., Yacoub, E., Olman, C. A., Auerbach, E., Strupp, J., Harel, N., & Ugurbil, K. (2010). Multiband multislice GE-EPI at 7 tesla, with 16-fold acceleration using partial parallel imaging with application to high spatial and temporal whole-brain FMRI. *Magnetic Resonance in Medicine*, *63*(5), 1144–1153. https://doi.org/10.1002/mrm.22361

Noll, D. C., Nishimura, D. G., & Macovski, A. (1991). Homodyne detection in magnetic-resonance-imaging. *IEEE Transactions on Medical Imaging*, *10*(2), 154–163. https://doi.org/10.1109/42.79473

Ogawa, S., Lee, T. M., Kay, A. R., & Tank, D. W. (1990). Brain magnetic resonance imaging with contrast dependent on blood oxygenation. *Proceedings of the National Academy of Sciences of the United States of America*, *87*(24), 9868–9872. https://doi.org/10.1073/pnas.87.24.9868

Pflugfelder, D., Vahedipour, K., Uludag, K., Shah, N. J., & Stocker, T. (2011). On the numerically predicted spatial BOLD fMRI specificity for spin echo sequences. *Magnetic Resonance Imaging*, *29*(9), 1195–1204. https://doi.org/10.1016/j.mri.2011.07.015

Press, W. H., Teukolsky, S. A., Vetterling, W. T., & Flannery, B. P. (1992). *Numerical recipes in C the art of scientific computing* (2nd ed., p. 994). Cambridge University Press.

Setsompop, K., Gagoski, B. A., Polimeni, J. R., Witzel, T., Wedeen, V. J., & Wald, L. L. (2012). Blipped-controlled aliasing in parallel imaging for simultaneous multislice echo planar imaging with reduced g-factor penalty. *Magnetic Resonance in Medicine*, *67*(5), 1210–1224. https://doi.org/10.1002/mrm.23097

Shah, N. J. (2015). Multimodal neuroimaging in humans at 9.4 T: A technological breakthrough towards an advanced metabolic imaging scanner. *Brain Structure & Function*, *220*(4), 1867–1884. https://doi.org/10.1007/s00429-014-0843-4

Shah, N. J., da Silva, N. A., & Yun, S. D. (2019). Perfusion weighted imaging using combined gradient/spin echo EPIK: Brain tumour applications in hybrid MR-PET. *Human Brain Mapping*, *42*, 4144–4154. https://doi.org/10.1002/hbm.24537

Shah, N. J. & Zilles, K. (2003). Verfahren zur Untersuchung eines Objekts mittels Erfassung des Ortsfrequenzraumes. DE 000019962845 C2.

Shah, N. J., & Zilles, K. (2004). Imaging process in the spatial frequency space and useful for examining the properties of object. *US 6781372 B2*.

Sharoh, D., van Mourik, T., Bains, L. J., Segaert, K., Weber, K., Hagoort, P., & Norris, D. G. (2019). Laminar specific fMRI reveals directed interactions in distributed networks during language processing. *Proceedings of the National Academy of Sciences of the United States of America*, *116*(42), 21185–21190. https://doi.org/10.1073/pnas.1907858116

Shirer, W. R., Ryali, S., Rykhlevskaia, E., Menon, V., & Greicius, M. D. (2012). Decoding subject-driven cognitive states with whole-brain connectivity patterns. *Cerebral Cortex*, *22*(1), 158–165. https://doi.org/10.1093/cercor/bhr099

Smitha, K. A., Akhil Raja, K., Arun, K. M., Rajesh, P. G., Thomas, B., Kapilamoorthy, T. R., & Kesavadas, C. (2017). Resting state fMRI: A review on methods in resting state connectivity analysis and resting state networks. *The Neuroradiology Journal*, *30*(4), 305–317. https://doi.org/10.1177/1971400917697342

Tian, P. F., Teng, I. C., May, L. D., Kurz, R., Lu, K., Scadeng, M., Hillman, E. M. C., De Crespigny, A. J., D'Arceuil, H. E., Mandeville, J. B., Marota, J. J. A., Rosen, B. R., Liu, T. T., Boas, D. A., Buxton, R. B., Dale, A. M., & Devor, A. (2010). Cortical depth-specific microvascular dilation underlies laminar differences in blood oxygenation level-dependent functional MRI signal. *Proceedings of the National Academy of Sciences of the United States of America*, *107*(34), 15246–15251. https://doi.org/10.1073/pnas.1006735107

van den Heuvel, M. P., & Hulshoff Pol, H. E. (2010). Exploring the brain network: A review on resting-state fMRI functional connectivity. *European Neuropsychopharmacology*, *20*(8), 519–534. https://doi.org/10.1016/j.euroneuro.2010.03.008

van der Zwaag, W., Buur, P. F., Fracasso, A., van Doesum, T., Uludag, K., Versluis, M. J., & Marques, J. P. (2018). Distortion-matched T1 maps and unbiased T1-weighted images as anatomical reference for high-resolution fMRI. *NeuroImage*, *176*, 41–55. https://doi.org/10.1016/j.neuroimage.2018.04.026

van Dijk, J. A., Fracasso, A., Petridou, N., & Dumoulin, S. O. (2020). Linear systems analysis for laminar fMRI: Evaluating BOLD amplitude scaling for luminance contrast manipulations. *Scientific Reports*, *10*(1), 5462. https://doi.org/10.1038/s41598-020-62165-x

van Mourik, T., van der Eerden, J. P. J. M., Bazin, P. L., & Norris, D. G. (2019). Laminar signal extraction over extended cortical areas by means of a spatial GLM. *PLoS One*, *14*(3), e0212493. https://doi.org/10.1371/journal.pone.0212493

Vazquez, A. L., Fukuda, M., Crowley, J. C., & Kim, S. G. (2014). Neural and hemodynamic responses elicited by forelimb- and photo-stimulation in channelrhodopsin-2 mice: Insights into the hemodynamic point spread function. *Cerebral Cortex*, *24*(11), 2908–2919. https://doi.org/10.1093/cercor/bht147

Vogt, C., & Vogt, O. (1919). *Allgemeine Ergebnisse unserer Hirnforschung*. Verlag von Johann Ambrosius Barth.

Vu, A. T., Jamison, K., Glasser, M. F., Smith, S. M., Coalson, T., Moeller, S., Auerbach, E. J., Ugurbil, K., & Yacoub, E. (2017). Tradeoffs in pushing the spatial resolution of fMRI for the 7T Human Connectome Project. *NeuroImage*, *154*, 23–32. https://doi.org/10.1016/j.neuroimage.2016.11.049

Walters, N. B., Eickhoff, S. B., Schleicher, A., Zilles, K., Amunts, K., Egan, G. F., & Watson, J. D. G. (2007). Observer-independent analysis of high-resolution MR images of the human cerebral cortex: In vivo delineation of cortical areas. *Human Brain Mapping*, *28*(1), 1–8. https://doi.org/10.1002/hbm.20267

Wielopolski, P., Schmitt, F., & Stehling, M. (1998). Echo-planar imaging pulse sequences. In *Echo-planar imaging* (pp. 65–139). Springer.

Wong, E. C. (1992). Shim insensitive phase correction for EPI using a two echo reference scan. *Paper presented at the ISMRM*. Nice, France.

Yu, X., Qian, C. Q., Chen, D. Y., Dodd, S. J., & Koretsky, A. P. (2014). Deciphering laminar-specific neural inputs with line-scanning fMRI. *Nature Methods*, *11*(1), 55. https://doi.org/10.1038/Nmeth.2730

Yun, S., Pais-Roldán, P., & Shah, N. J. (2020). Detection of cortical depth-dependent functional activation using whole-brain, half-millimetre resolution EPIK at 7T. *Paper presented at the ISMRM*.

Yun, S., & Shah, N. J. (2019). Full-FOV, whole-brain, half-millimetre resolution fMRI at 7T using accelerated multi-band EPIK with TR-external phase correction. *Paper presented at the ISMRM*. Montreal, Canada.

Yun, S. D., Reske, M., Vahedipour, K., Warbrick, T., & Shah, N. J. (2013). Parallel imaging acceleration of EPIK for reduced image distortions in fMRI.

NeuroImage, *73*, 135–143. https://doi.org/10.1016/j.neuroimage.2013.01.070

Yun, S. D., & Shah, N. J. (2017). Whole-brain high in-plane resolution fMRI using accelerated EPIK for enhanced characterisation of functional areas at 3T. *PLoS One*, *12*(9), e0184759. https://doi.org/10.1371/journal.pone.0184759

Yun, S. D., & Shah, N. J. (2020). Analysis of EPI phase correction with low flip-angle excitation to reduce the required minimum TE: Application to whole-brain, submillimeter-resolution fMRI at 3 T. *Magnetic Resonance in Medicine*, *84*, 1416–1429. https://doi.org/10.1002/mrm.28218

Yun, S. D., Weidner, R., Weiss, P. H., & Shah, N. J. (2019). Evaluating the utility of EPIK in a finger tapping fMRI experiment using BOLD detection and effective connectivity. *Scientific Reports*, *9*(1), 10978. https://doi.org/10.1038/s41598-019-47341-y

Zaitsev, M., D'Arcy, J., Collins, D. J., Leach, M. O., Zilles, K., & Shah, N. J. (2005). Dual-contrast echo planar imaging with keyhole: Application to dynamic contrast-enhanced perfusion studies. *Physics in Medicine and Biology*, *50*(19), 4491–4505. https://doi.org/10.1088/0031-9155/50/19/005

Zaitsev, M., Zilles, K., & Shah, N. J. (2001). Shared k-space echo planar imaging with keyhole. *Magnetic Resonance in Medicine*, *45*(1), 109–117. https://doi.org/10.1002/1522-2594(200101)45:1<109::aid-mrm1015>3.0.co;2-x

Zhang, H., Shen, D. G., & Lin, W. L. (2019). Resting-state functional MRI studies on infant brains: A decade of gap-filling efforts. *NeuroImage*, *185*, 664–684. https://doi.org/10.1016/j.neuroimage.2018.07.004

Zilles, K., Palomero-Gallagher, N., & Amunts, K. (2015). Myeloarchitecture and maps of the cerebral cortex. In *Brain mapping: An encyclopedic reference* (pp. 137–156). Elsevier Academic Press.

Zimmermann, J., Goebel, R., De Martino, F., van de Moortele, P. F., Feinberg, D., Adriany, G., Chaimow, D., Shmuel, A., Ugurbil, K., & Yacoub, E. (2011). Mapping the organization of axis of motion selective features in human area MT using high-field fMRI. *PLoS One*, *6*(12), e28716. https://doi.org/10.1371/journal.pone.0028716

Zong, X., Lee, J., John Poplawsky, A., Kim, S. G., & Ye, J. C. (2014). Compressed sensing fMRI using gradient-recalled echo and EPI sequences. *NeuroImage*, *92*, 312–321. https://doi.org/10.1016/j.neuroimage.2014.01.045

SUPPORTING INFORMATION

Additional supporting information may be found in the online version of the article at the publisher's website.

How to cite this article: Yun, S. D., Pais-Roldán, P., Palomero-Gallagher, N., & Shah, N. J. (2022). Mapping of whole-cerebrum resting-state networks using ultra-high resolution acquisition protocols. *Human Brain Mapping*, *43*(11), 3386–3403. https://doi.org/10.1002/hbm.25855